Thermal excitation in a spatially modulated monolayer solid: Incommensurate xenon/graphite

A. D. Novaco*
Department of Physics, Lafayette College Easton, Pennsylvania 18042, USA

L. W. Bruch†
Department of Physics, University of Wisconsin–Madison, Madison, Wisconsin 53706, USA
(Received 3 December 2013; revised manuscript received 12 March 2014; published 31 March 2014)

Calculations of the properties of monolayer xenon/graphite for temperatures up to its triple point at 100 K are reported. The average lattice constant and orientational epitaxy angle for the monolayer solid are evaluated along its (two-dimensional) sublimation curve. The incommensurate rotated lattice approaches the incommensurate aligned configuration as the melting temperature is approached, as in experiments. The calculated temperature, latent heat of melting, and solid-liquid density difference at the triple point agree with experiment. The methods include molecular dynamics simulations for large submonolayer patches of xenon and both self-consistent-phonon and perturbation-variation approximations. An overall quantitative agreement between the simulations, calculations, and experimental data is achieved with an interaction model that includes the spatially periodic xenon-graphite corrugation energy.

DOI: 10.1103/PhysRevB.89.125431 PACS number(s): 68.43.−h, 64.70.−p, 68.43.De

I. INTRODUCTION

A great deal is known [1,2] about the monolayer solid of xenon adsorbed on the basal plane of graphite, Xe/graphite, but the possible importance of substrate corrugation effects has obscured [3] the relation of this system to melting phenomena predicted for two-dimensional (2D) solids [4]. Previously [5], we examined the conditions for stability of the commensurate $(\sqrt{3} \times \sqrt{3})R30^\circ$ lattice of Xe/graphite that is a compressed phase of the monolayer solid. A quantitative account of the stability of the commensurate lattice at temperatures near 60 K was achieved [5] by adjusting the leading amplitude V_g in the spatially periodic Xe-graphite potential energy (the corrugation energy). The calculations reproduced the experimental low-temperature lattice constant at monolayer condensation L_u. Here, we evaluate the properties predicted by that model for the solid at higher temperatures. Effects of V_g are small in much of the phase diagram. Some experimental data, such as the values for L_u at 60 to 100 K and the main features of the triple-point melting at 100 K, are reproduced and are insensitive to V_g. However, orientational epitaxy and the commensurate solid arise only because there is a surface corrugation $V_g \neq 0$.

In orientational (also termed "rotational") epitaxy [6], the monolayer solid lattice is aligned at an angle ϑ to a symmetry axis of the substrate. The energetics of mass density waves (MDW) determine ϑ and, generally, there is a threshold misfit [7] to go from an incommensurate aligned (IA) state to an incommensurate rotated (IR) $\vartheta \neq 0$ state [8]. Experimental data [2] for Xe/graphite show an unusual succession of IA, IR, and finally IA states as the misfit increases, but there are scarcely any applications of theory and simulation to this problem. Our molecular dynamics (MD) results show that the orientational epitaxy angle ϑ decreases with increasing temperature near the monolayer melting temperature, in agreement with experiment [9], although perturbation theory [6] predicts that ϑ increases because thermal expansion increases the misfit. The balance in the competition between interior physics (MDW) and boundary physics/edge effects changes with system size [10].

We have implemented an array of computational methods to get a quantitative account of structures and dynamics in regions of the monolayer phase diagram with large thermal excitation. We use MD simulations for the temperature range between harmonic solid conditions and the triple-point melting of submonolayer Xe/graphite. The MD simulations are extended to large Xe islands to reduce a bias introduced by smaller constrained cells. The largest island in the simulations has 312 000 atoms and this is on the scale of the largest coherent patches in Xe/graphite experiments [11]. We examine the modulation energy E_{MDW} of the mass density waves by several approximations as it is the driver of orientational epitaxy. The threshold misfit for the IA → IR transition is determined with a perturbation-variation (PV) extension of the Novaco-McTague perturbation theory [6]. The self-consistent phonon (SCP)-MDW approximation [5,12,13] was used as a check on the MD and PV work.

The computer simulations most closely related to our Xe/graphite work are a Monte Carlo simulation of monolayer Ar/graphite by Flenner and Etters [14] that allows for three-dimensional (3D) motion of the argon atoms and a molecular dynamics simulation for a large 2D array of generic Lennard-Jones [LJ] atoms near its triple-point temperature T_t by Asenjo *et al.* [15]. Experiments [16,17] strongly suggest that triple-point melting of Ar/graphite is a continuous transition while that of Xe/graphite is first order. Flenner and Etters treated samples of 256 to 1600 argon atoms and found a continuous melting transition with phenomena near T_t that are strongly affected by the graphite corrugation. They also found, in agreement with early work of Abraham [18], that a 2D treatment is a good approximation to their 3D results for submonolayer coverage and small spreading pressure. Asenjo *et al.* treated relatively large samples of 36 864 LJ(12,6) atoms with no corrugation potential and found triple-point behavior that is consistent with first-order melting. Our

*novacoad@lafayette.edu
†lwbruch@wisc.edu

calculations are 2D simulations using a realistic potential model for submonolayer Xe/graphite and including substrate corrugation, with arrays of 78 000 and 312 000 xenon atoms. A surprising result is that our triple-point temperature and latent heat of melting are close to values obtained by scaling the Asenjo *et al.* results. This occurs in spite of the fact that the calculated orientational epitaxy shows effects of the substrate corrugation (V_g) near T_t but it is consistent with the fact that the calculated T_t and latent heat remain very similar for a range of V_g. The differences between Ar/graphite and Xe/graphite in simulations and in experiments are in contrast to the successful applications of corresponding states [2] scaling for 3D argon and xenon and highlight the delicate balances involved in monolayer melting. We have been able to explain the remarkable experimental results [9] for the evolution of the orientational epitaxy angle ϑ along the monolayer sublimation curve of Xe/graphite.

The organization of this paper is as follows. Section II contains a description of the components and tests of the calculation and Sec. III the application to Xe/graphite. Concluding remarks are given in Sec. IV. There are three Appendices: Appendix A, the implementation of the MD; Appendix B, useful surrogates; and Appendix C, the perturbation-variation (PV) approximation to orientational epitaxy. See Ref. [19] for Supplemental Material.

II. COMPONENTS OF THE CALCULATION

A. Interactions and samples

The interaction model is the same as in Paper I [5]. This is a 2D calculation in which the xenon positions are constrained to lie in a plane above the triangular Bravais lattice ($\ell = 2.46$ Å) of the graphite surface. The Xe-Xe HFD-B2 pair potential [20] ($\epsilon = 282.8$ K; $R_{\min} = 4.3635$ Å) is augmented by the McLachlan substrate-mediated dispersion energy [21] with parameters $C_{s1} = 142$ au, $C_{s2} = 89$ au, and overlayer height $L_{ov} = 1.9$ Å, so that the minimum in the effective pair potential is -244.8 K at a separation 4.400 Å. The corrugation potential energy is parametrized using only the first shell of six reciprocal lattice vectors $\mathbf{g}$ of the graphite $|\mathbf{g}| = g_0 = 4\pi/\ell\sqrt{3}$ [22]:

$$V_s(\mathbf{r}) = V_g \sum_{\mathbf{g}} \exp(\imath \mathbf{g}\cdot\mathbf{r}). \tag{1}$$

The origin of $\mathbf{r}$ is at the center of a carbon hexagon and three values of V_g [namely, -5.0, -6.0, and -7.0 K] are used. This V_g span gives chemical potential stability margins [5] for the commensurate phase that agree with the experimental phase diagram [1,2]. $V_g = -6$ K has been used as the "best estimate" fitting a range of data at temperatures $T < 60$ K.

The simulations treat unconstrained xenon arrays consisting of an "island" or patch that fills about 50% of the simulation cell. This avoids a bias on the orientational epitaxy introduced by periodic boundary conditions. The quite large patches allow for the growth of correlation lengths near the melting and reduce the fractional effect of boundary terms. Most of the work has a hexagonal solid patch of 78 000 atoms ("78 K") as the initial configuration; there also is a series of calculations with a patch of 312 000 atoms ("312 K") for $V_g = -6$ K. In Paper I, the largest patch had 20 064 ("20 K") atoms.

The specification of the parameters for the models in the figures is given as SW*X*H.HFD-B2.McL.*Y*, where *X* gives the magnitude of V_g in Kelvin and *Y* the size of the patch (78 K or 312 K). The rest of the label specifies that the corrugation [Eq. (1)] is a harmonic sine wave (SW), the patch is hexagonal (H), and pair interactions are the HFD-B2 potential augmented by the McLachlan substrate-mediated interaction (McL).

B. Methods

The basic tool is a classical molecular dynamics (MD) simulation in the standard NVE ensemble [23] (Appendix A). The temperature is derived from the average kinetic energy $\langle K\rangle$. Because a low-density 2D gas coexists with the solid, the simulation has similarities to an NPT simulation of the 2D sublimation curve. The work reported here had a substantial commitment of computational resources amounting to more than 150 CPU years with server class processors having clock speeds in the 2.4 to 3.0 GHz range.

We evaluate the thermal average potential energy $\langle\Phi\rangle$, structure factor $S(\mathbf{q})$, and hexatic (Nelson-Halperin) order parameter [4,24,25] ψ_6:

$$\psi_6 = \left\langle \frac{\sum_{ij} \exp(\imath 6\theta_{ij})}{\sum_{ij} 1} \right\rangle. \tag{2}$$

θ_{ij} is the angle that the relative position vector $\mathbf{r}_j - \mathbf{r}_i$ makes with the $\mathbf{g}(10)$ reciprocal lattice vector of the graphite for adatom pairs at separations up to $1.41 - 1.49R_{\min}$ to span the first-neighbor shell, i.e., within a disk in the monolayer solid that usually contains 7 Xe. (This way of determining the first-neighbor shell is not as systematic as that of other workers [15,26–28] who used a Voronoi construction or Delaunay triangulation.) Melting is manifested by a steep continuous drop in $|\psi_6|$ as a function of temperature, but a "tail" persists above the melting temperature for the corrugated surface $V_g \neq 0$, as shown in Fig. 1.

The structure factor $S(\mathbf{q})$ for the N-atom patch,

$$S(\mathbf{q}) = \left\langle \left| \sum_{j=1}^{N} \exp(\imath \mathbf{q}\cdot\mathbf{r}_j) \right|^2 \right\rangle \Big/ N^2, \tag{3}$$

is evaluated for grids of wave vectors $\mathbf{q}$ to locate peaks. The largest peaks occur at the reciprocal lattice vectors $\boldsymbol{\tau}$ of the average lattice except at temperatures within 0.5 K of the melting temperature, where the density modulation driven by $V_s(\mathbf{r})$ creates stronger peaks at $\mathbf{g}(10)$ than at $\boldsymbol{\tau}$. The $\boldsymbol{\tau}$ give both the spacing L_{nn} and the orientation ϑ of the average lattice (Appendix B). The peak heights of $S(\mathbf{q})$ decrease sharply (Fig. 2) in the same T range as the drop in $|\psi_6|$; both drops occur in a temperature range of about 1 K.

We use variants of the self-consistent-phonon (SCP) approximation, especially the self-consistent-phonon mass-density-wave (SCP-MDW) approximation for spatially nonuniform monolayer lattices [5,12,13]. Potential energies of nonuniform monolayer lattices also are evaluated with force-relaxation energy minimizations on higher-order-commensurate (HOC) lattices [5] as in Paper I and with

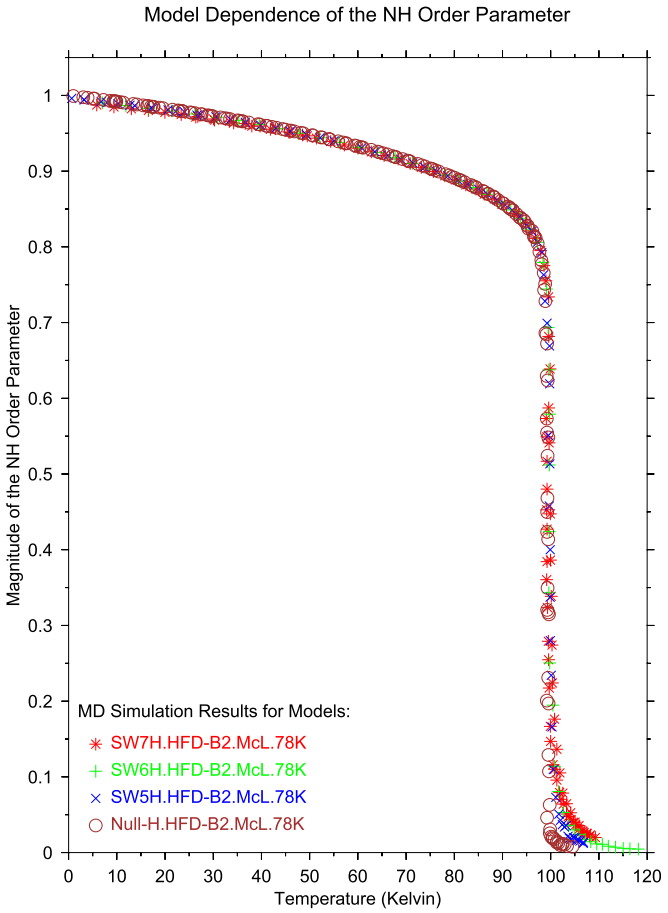

FIG. 1. (Color online) Hexatic order parameter ψ_6 as function of temperature T. The magnitude $|\psi_6|$ is plotted for simulations of the 78 K patch using four values of V_g (0, −5, −6, and −7 K) [Eq. (1)]. Note that the curves essentially superpose except for the tail above the melting transition at $T \simeq 100$ K.

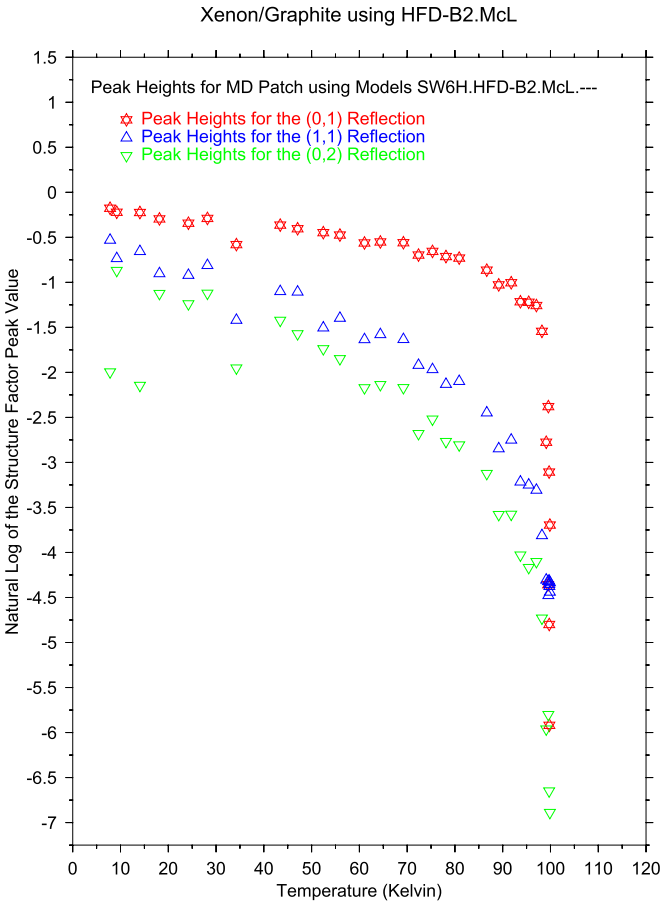

FIG. 2. (Color online) Temperature dependence of $\ln S(\tau)$ for the (0,1), (1,1), and (0,2) reciprocal lattice vectors of the 78 K patch with $V_g = -6$ K. S is normalized by $1/N^2$ [Eq. (3)].

a generalization (PV) of the perturbation theory [6] of the nonuniform lattice that is outlined in Appendix C.

As a measure of the lateral stress on the monolayer, we evaluate an effective pressure P_v using the virial theorem [29]. The 2D pressure P_v for N particles in area A at temperature T is given by

$$P_v A = N k_B T - \frac{1}{2}\sum_j \langle \mathbf{r}_j \cdot \nabla_j V_s(\mathbf{r}_j)\rangle - \frac{1}{4}\sum_{i\neq j}\langle (\mathbf{r}_j - \mathbf{r}_i)\cdot \nabla_j \phi(r_{ij})\rangle. \quad (4)$$

In Eq. (4), the classical equipartition theorem for the kinetic energy is used and the internal virial is evaluated in terms of the forces from the corrugation energy [Eq. (1)] and the adatom pair potentials $\phi(r_{ij})$. The time average $\langle \cdots \rangle$ is evaluated with the MD simulation; results are shown in Fig. 3. Also, in the temperature range 85–100 K, for which appreciable 2D gas coexists with the solid patch, we determine the populations of small clusters by finding the numbers of adatoms that have on average $0, 1, 2, \ldots$ neighbors within a radius $R \simeq 6.4$ Å.

C. Tests

We made several tests to assure ourselves that the implementation of the MD simulation was reliable. Side calculations with more elementary methods showed quantitative agreement for the nearly harmonic low-temperature solid and had the expected departures at higher temperatures.

1. Lattice constants

Monte Carlo simulations showed [30] that the lattice constant of monolayer Xe on a structureless substrate can be reproduced by near-analytical approximations [quasiharmonic lattice theory (QHT) and cell models] over the temperature range 0–95 K. Now, we compare the temperature-dependent lattice constant $L_u(T)$ of an unconstrained patch, determined from the MD data for the peaks of $S(\mathbf{q})$, to the results of the following calculations: the classical limit ($\hbar \to 0$) of QHT below 40 K; the SCP-MDW approximation over the temperature range 0–80 K; and the classical cell approximation for 50–95 K. In the temperature ranges of their anticipated applicability, these approximations reproduced the MD results to within about 0.01 Å.

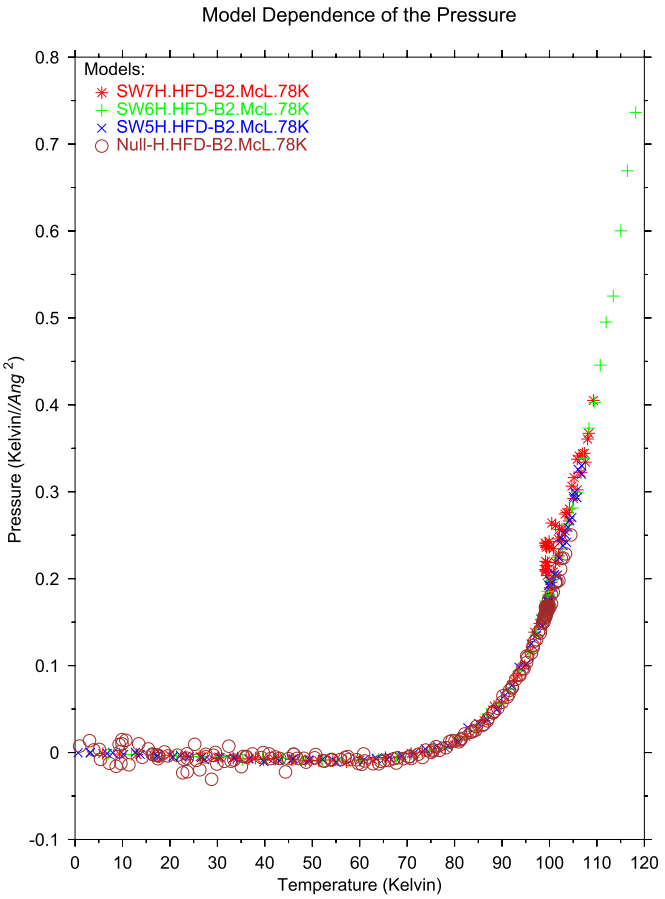

FIG. 3. (Color online) Virial pressure P_v as a function of temperature T along the 2D sublimation curve for $V_g = 0, -5, -6, -7$ K (78 K patch). P_v is evaluated using Eq. (4). For the $V_g = -6$ K 312 K patch results, see the Supplemental Material [19].

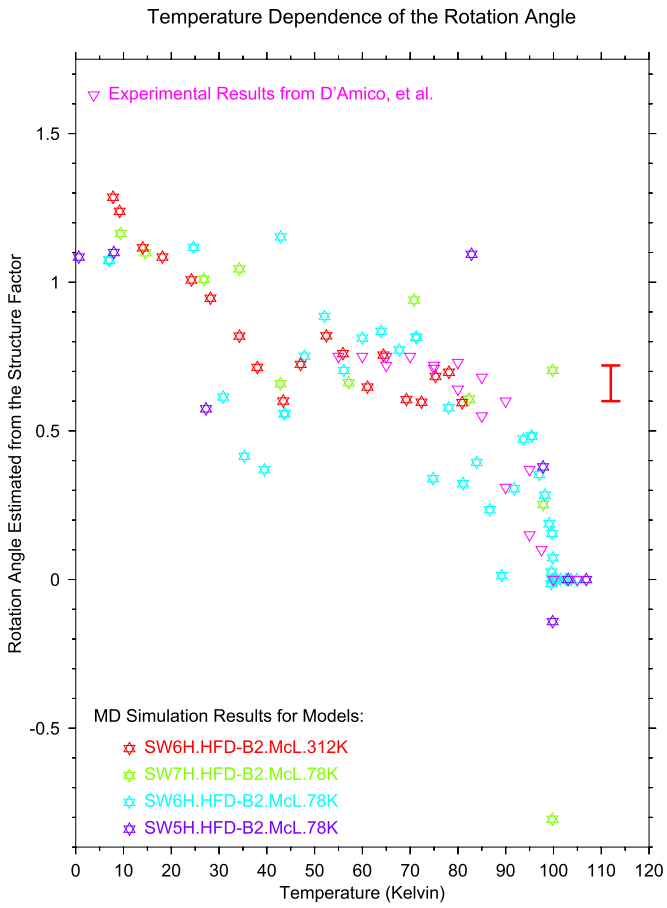

FIG. 4. (Color online) Orientational epitaxy angle ϑ as a function of temperature T for $V_g = -5, -6, -7$ K (78 K patch) and for $V_g = -6$ K (312 K patch). ϑ is given in degrees relative to the $\sqrt{3}$ axis of the graphite. Data of D'Amico *et al*. [9]. The uncertainty in the calculated ϑ is believed to be $\pm 0.1^\circ$; see the discussion in Appendix A. The error bar on the right of the figure represents the maximum range of values for ϑ based on the four $S(\mathbf{q})$ peaks used.

2. *Modulation energy*

The energy E_{MDW} arising from mass density waves is the increment in thermal average total energy driven by $V_g \neq 0$. The MD work has signs that the orienting effect of E_{MDW} becomes weaker at temperatures above about 60 K. For instance, the orientational epitaxy angle ϑ in Fig. 4 stops decreasing with increasing temperature (and misfit) at about 60 K and then is roughly constant until close to melting. The relaxation time for ψ_6 also increases as the melting is approached. As the temperature increases, $|E_{\mathrm{MDW}}|$ is expected to decrease as a consequence of the increasing misfit that arises from thermal expansion and of the averaging of $V_s(\mathbf{r})$ that arises from the thermal motion. We made several tests that the thermal-average values for E_{MDW} evolve in the expected way.

The total potential energy Φ for the $T \to 0$ K limit of the MD calculations was constructed for both the 78 K and 312 K patches with $V_g = -6$ K and for the 78 K patch with $V_g = -5$ K. A combination of the PV and HOC calculations reproduces the $\Phi \simeq -780$ K of the 312 K $V_g = -6$ K case to 0.1 K. For the two 78 K cases, the MD energy is about 0.8 K more negative, suggesting the difference arises from the neglect of relaxation at the patch edge in the PV approximation. The static lattice $|E_{\mathrm{MDW}}|$ decreases in the expected way as L_{nn} increases. Some results for $V_g = -6$ K, evaluated for higher-order-commensurate (HOC) unit cells, are shown in Table I. These results and their approximation by the perturbation-variation (PV) calculation are discussed further in Appendix C.

Another estimate of E_{MDW} uses two configurations of the 312 K patch ($V_g = -6$ K) at $T \simeq 10$ K that remained at $\vartheta \simeq 1^\circ$ and 15° for long times. The lattice constant $L_{nn} = 4.375$ Å is reproduced to 0.01 Å by the QHT and the energy difference between the two MD calculations is 6.5 K while the PV approximation gives about 5.5 K for the energy difference of the two alignments. We consider this to be satisfactory agreement because the PV approximation underestimates the HOC value for E_{MDW} by 0.85 K at $L = 4.373$ Å, as shown in the Supplemental Material [19].

The effect of thermal averaging on E_{MDW} for a given V_g and L_{nn} is shown by the SCP-MDW approximation (Fig. 5). There is a reduction of more than 50% in E_{MDW} as the temperature increases from 0 to 60 K, but the energy difference between the $\sqrt{3}$ alignment and the optimum angle remains about 0.1 K for $L = 4.40$–4.45 Å. That is, the SCP-MDW approximation shows two qualitative features of E_{MDW}. First, there is a rather small variation in E_{MDW} for $0 \leqslant \vartheta \leqslant 1^\circ$. Second, the

TABLE I. Approximations to the mass density wave energy E_{MDW}. Configurations specified by lattice constant L, alignment ϑ, and the number N of adatoms in the HOC unit cell. Sets of higher-order-commensurate (HOC) lattice cells, rotated and aligned, at nearly the same L are listed. Calculations for the HFD-B2 + McLachlan effective pair potential and $V_g = -6$ K. E_{MDW} is from a force relaxation on the HOC cell; E(PV) is from a perturbation-variation calculation on the average triangular lattice patch of 78 000 atoms. Lengths are in Å and energies (per adatom) are in Kelvin. The misfits are 3.8%–7.2% and correspond to states on the sublimation curve.

L	ϑ[a]	N	E_{MDW}	E(PV)	E(PV) − E_{MDW}	%	E_{NM}[b]
4.5656	0.7351	441	−2.542	−2.417	0.125	4.92	−2.449
4.5652	0	196	−2.521	−2.393	0.128	5.08	−2.415
4.5298	1.945	64	−2.677	−2.573	0.104	3.88	−2.635
4.5274	0.648	576	−2.656	−2.540	0.116	4.37	−2.567
4.5271	0	256	−2.631	−2.516	0.115	4.37	−2.522
4.5168	0.624	625	−2.716	−2.599	0.117	4.31	−2.626
4.5115	0	289	−2.723	−2.608	0.115	4.23	−2.608
4.4996	1.74	81	−2.891	−2.842	0.049	1.69	−2.868
4.4976	0	324	−2.832	−2.711	0.121	4.27	−5.282
4.4756	1.575	100	−3.159	−3.027	0.132	4.18	−3.155
4.4741	0.525	900	−3.121	−2.981	0.140	4.49	−3.020
4.4739	0	400	−3.090	−2.953	0.137	4.43	−2.954
4.4559	1.438	121	−3.465	−3.335	0.130	3.75	−3.486
4.4545	0	484	−3.392	−3.233	0.159	4.69	−3.238
4.4396	1.323	144	−3.803	−3.615	0.188	4.94	−3.854
4.4384	0	576	−3.728	−3.536	0.192	5.15	−3.556
4.4257	1.225	169	−4.167	−4.009	0.158	3.79	−4.255
4.4247	0	676	−4.095	−3.857	0.238	5.81	−3.906

[a]Angles in degrees relative to the 30° commensurate alignment of graphite. 0° is incommensurate aligned (IA) while $\vartheta \neq 0$ is incommensurate rotated (IR).

[b]Second-order perturbation theory value for E_{MDW}, following Novaco and McTague [6].

overall effect of the MDW terms decreases with increasing temperature. Most of the increment in $E_{\mathrm{MDW}}(\vartheta)$ occurs for ϑ in the range 2°–10° and there is only a relatively small change between 12° and 30°, as in the results of the original perturbation theory [6].

Finally, we estimated E_{MDW} at temperatures 60–85 K by comparing $\langle\Phi\rangle$ for the MD calculations ($V_g = -6$ K) to the average energy found in Null continuations of the MD calculations. Then, an equilibrated configuration (and kinetic energy) was used as the starting configuration and V_g was set to zero. By choosing temperatures above 60 K, the lattice constants for the Null and V_g cases are the same to ±0.01 Å at a given temperature. We use a spline calculation to interpolate in the Null cases to the temperature of a V_g case and then take the modulation energy to be the difference in the two values of $\langle\Phi\rangle$. The ratio of the estimated modulation energy to E_{MDW} calculated with the PV approximation at the same lattice constant decreases from 0.7 at 60 K to 0.5 at 85 K. The scale of the reduction and the trend with temperature agree with what we expect from the SCP-MDW approximation and with the trend inferred from the MD results for ϑ.

3. Size dependence

Our most extensive calculations are with the 78 K patch. We also made a scan over temperature for the 312 K patch at $V_g = -6$ K. A comparison of the 78 K and 312 K results for the total energy $\langle E\rangle = \langle K + \Phi\rangle$ is shown in Fig. 6; the corresponding graphs for the magnitude of the hexatic order parameter $|\psi_6|$ and the virial pressure P_v are shown in the Supplemental Material [19]. Total energies varied with patch size in an understood manner. The 312 K values for ϑ as a function of temperature (Fig. 4) showed smaller fluctuations/scatter than the results for the 78 K patch, and we take this as further evidence of the sensitivity of ϑ to details of the calculation. Our results for the 20 K patch, not shown here, also had large fluctuations, no clear pattern, and little resemblance either to the experimental results or to the simulation results for the 78 K and 312 K patches.

The alignments ϑ are driven mostly by E_{MDW}, but a second mechanism becomes important for small patches. Then, there is a net value for V_s even when summed over the rigid uniform adlayer. The optimum ϑ typically is in the range 1°–2° and both ϑ and the ratio $\langle V_s\rangle / V_g$ are sensitive to system size N. Figure 7 shows how the V_s contribution for a rigid hexagonal patch varies with system size for three values of the scaled density $\rho/\rho_{\sqrt{3}}$, where $\rho_{\sqrt{3}}$ is the density of a perfect commensurate lattice. This rigid lattice calculation gives one limit for the competition between boundary effects and interior effects as calculated by the MDW-SCP approach. With $V_g = -5$ K, the rigid lattice energy becomes larger than $E_{\mathrm{MDW}} = -4.1$ K at $L = 4.38$ Å for $N < 400$ and −1.8 K at $L = 4.52$ Å for $N < 1000$ (see Fig. 7).

4. Hysteresis and relaxation

We have used two tests of equilibration in the simulation: the size of hysteresis effects and the correlation time of time-block averages of the kinetic energy. By hysteresis we mean that averages do not retrace their values as a function of temperature when cooling after a heating series. This effect is small, as the offset of E as a function of temperature is less

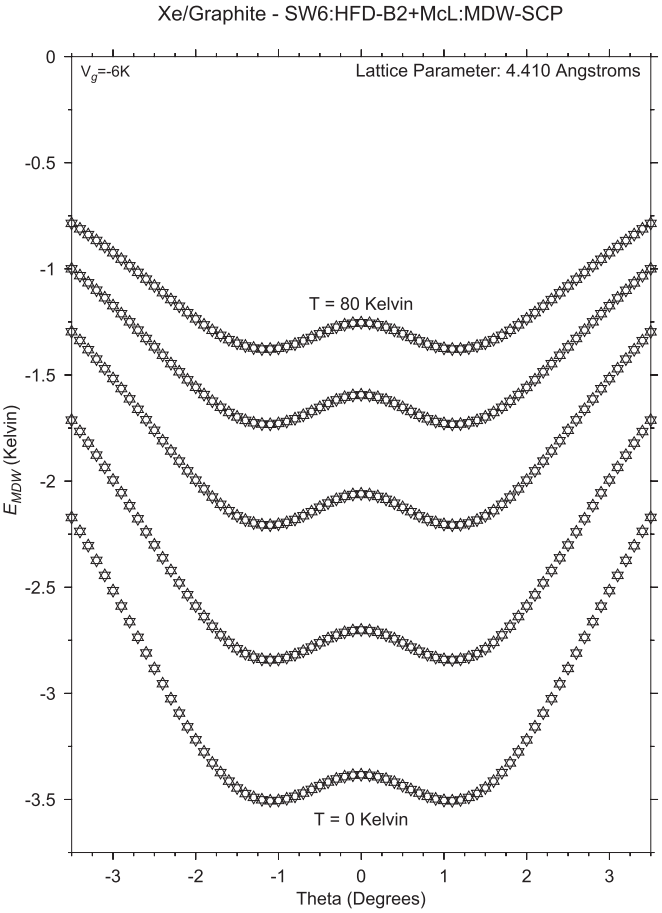

FIG. 5. SCP-MDW results for $E_{\mathrm{MDW}}(\vartheta)$ for $V_g = -6$ K at $L = 4.41$ Å; $T = 0,20,40,60,80$ K.

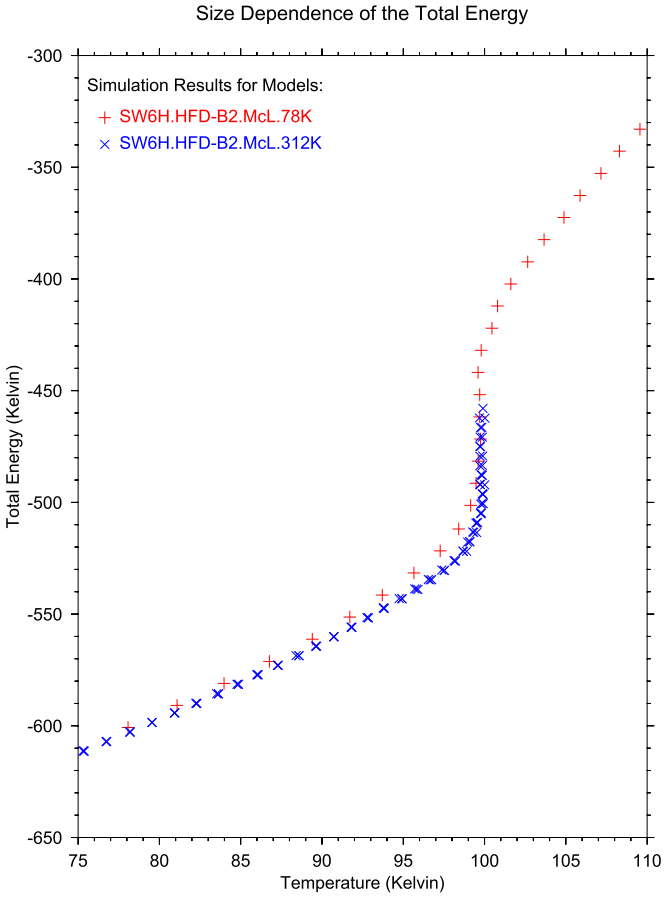

FIG. 6. (Color online) Total energy $E = \langle K + \Phi \rangle$ as a function of temperature for two patch sizes (78 K and 312 K) and $V_g = -6$ K. The cell average density is $\rho R_{\mathrm{min}}^2 \simeq 0.53$.

than 1 K (Fig. 8), with averages typically taken over 100 time blocks after 400 time blocks to relax to equilibrium; a similar graph for $|\psi_6|$ is shown in the Supplemental Material [19]. The nature of the hysteresis is that voids and large islands persist when the solid reassembles from the liquid.

The block averages also extend well beyond any transients. Relaxation times τ are determined by autocorrelation functions of the block averages of the temperature. After the first 400 blocks (time $4000t_0$), τ corresponds to about 20 blocks or less ($\leqslant$650 ps) so that the averages over blocks 400–500 are equilibrium averages (Fig. 9). These values are for the 78 K patches at a temperature near 100 K, close to the melting [31]. Asenjo *et al.* [15] found greatly increased relaxation times at temperatures within 1% of melting, and in some of our runs in this temperature range the relaxation times are larger than indicated in Fig. 9. The autocorrelation function for a quantity X was evaluated with [24]

$$C_{nXX}(t_1) = \frac{[\langle X(t_1+t_n)X(t_n)\rangle_n - \langle X(t_1+t_n)\rangle_n \langle X(t_n)\rangle_n]}{[\langle X(t_m)X(t_m)\rangle_m - \langle X(t_m)\rangle_m \langle X(t_m)\rangle_m]}, \tag{5}$$

where $\langle \ldots \rangle_m$ denotes an average over m blocks. In a typical calculation, a contiguous set of block averages was chosen. The average in the denominator was taken over all the blocks in that range, while in the numerator the average was taken over a fixed number n of blocks and the range of t_1 was set by the difference in the numbers of blocks in the numerator and denominator. $C_{XX}(t_1)$ as a function of t_1 is plotted in Fig. 9, with t_1 equal to the time at the center of a block of width 32.6 ps.

Figure 10 shows the relaxation of the orientational angle as a function of time for various initializations ϑ_i at a relatively low temperature $T \simeq 10$ K, far below the melting temperature. The case that was initialized at $\vartheta_i = 0^\circ$ maintained that orientation for the entire run of 500 blocks. The cases that were initialized at $\vartheta_i = 1^\circ$–13° all relaxed to a final orientation $\vartheta_f = 1.0^\circ$–1.5° within 500 blocks, although the larger ϑ_i required more time to reach this orientation. The two largest ϑ_i shown did not relax within the 500-block period. These behaviors are consistent with a function [6,12] $E_{\mathrm{MDW}}(\vartheta)$ that has a rather flat minimum near 1°, a steep increase between roughly 2° and 12°, and then a relatively flat plateau for 12° to 30°. To test how the temperature affects the relaxation time, many of these cases were repeated at temperatures where ϑ_f versus T shows a plateau, specifically at 53–58 K, and the equilibrium was disturbed by rotating the lattice away from the equilibrium orientation ($\simeq 1^\circ$) to initial orientations $\vartheta_i = 2^\circ$–9°; the results are shown in the Supplemental Material [19]. The case with $\vartheta_i \simeq 2^\circ$ showed little sign of any relaxation; cases with $\vartheta_i = 3^\circ$–9° did relax to smaller angles, but the relaxation times were much longer than the 250 blocks that were evaluated. We

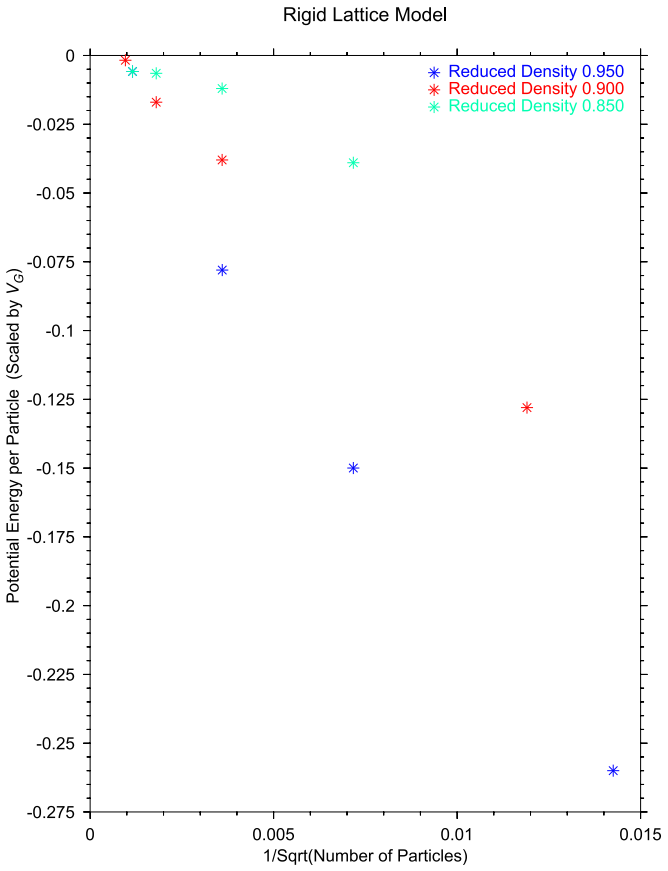

FIG. 7. (Color online) The scaled modulation energy $E_{\mathrm{MDW}}/|V_g|$ as a function of the (reciprocal) patch dimension $1/\sqrt{N}$, where N is the number of atoms in the patch, for three reduced densities $\rho/\rho_{\sqrt{3}}$. The energy E_{MDW} is the minimum corrugation potential energy after the placement and orientational alignment of the rigid triangular monolayer lattice are optimized on the surface.

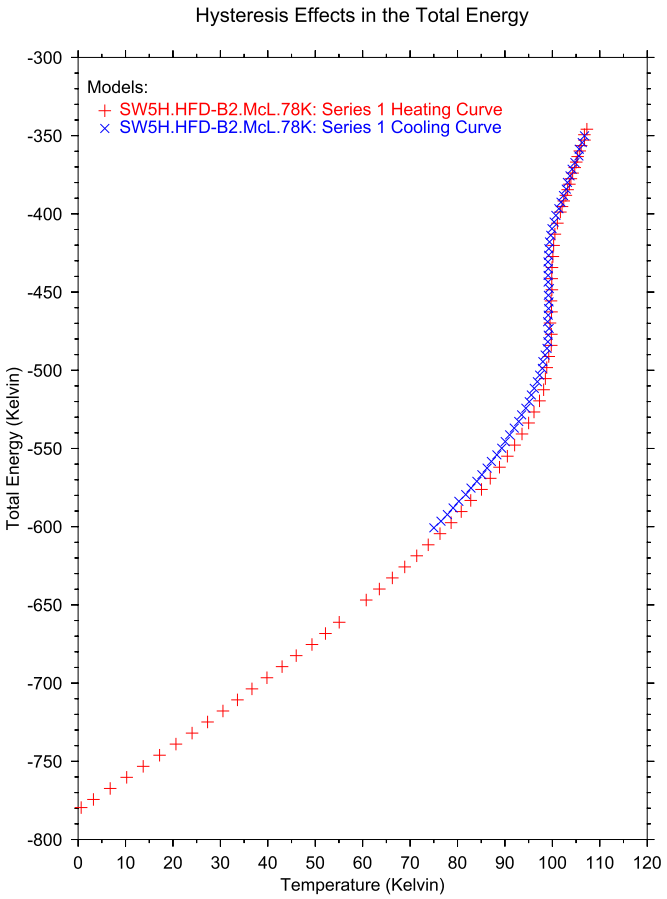

FIG. 8. (Color online) Hysteresis for the total energy E. Heating and cooling series near $T = 100$ K. Runs with 500 blocks, averages over last 100 blocks. $V_g = -5$ K and 78 K patch. The statistical uncertainties in the energy on the heating and cooling curves are on the order of ± 0.02 K and are much smaller than the systematic errors ($\sim$1 K) arising from incomplete equilibration, i.e., hysteresis effects.

view this as further evidence that the MDW energy plays much less of a role at the higher temperatures.

An effect very similar to kinetic slowing near the melting has placed a computational limit on our study of the 312 K system. As is evident in several of the figures, we were not able to follow this larger system through the melting transition. What happens is that the adatom configurations change so rapidly that the neighbor list for the MD force calculation has to be reconstructed at shorter time intervals and this slows the computation drastically. Cases with relaxation times longer than 10 ns would appear to us to be equilibrium states because there are unavoidable drifts in the total energy over such times in our MD implementation.

III. MODEL CALCULATIONS AND EXPERIMENT

A. Summary of experimental data

The triple-point temperature of monolayer Xe/graphite (i.e., melting point on the 2D sublimation curve) is [32] $T_t = 99$–100 K. Two analyses of the adsorption isotherms of Thomy *et al.* [33,34] place T_t at 99 and 100 K, respectively. The specific-heat data of Litzinger and Stewart [35] place it close to 100 K. The x-ray data of Hammonds *et al.* [36] show solidlike diffraction at 99 K but not at 100 K and are consistent with the thermodynamic data. Assignment of the triple-point melting of Xe/graphite as a first-order phase transition [16] is supported by observations of a density discontinuity [33,37,38] and two-phase coexistence [39] at the melting curve near T_t.

Thomy *et al.* [34] and Tessier [37] derived integral heats of adsorption $[q_s, q_v, q_m]$ for the sublimation, vaporization, and melting curves from the adsorption isotherm data. We adopt $q_s = 2766 \pm 50$ K, $q_v = 2567 \pm 50$ K, and $q_m = 3470 \pm 40$ K and hence have differences $q_m - q_s \simeq 704 \pm 65$ K and $q_m - q_v \simeq 903 \pm 70$ K. The thermodynamic analysis of Larher [40] relates the differences to the enthalpies (h) and densities (ρ) of coexisting liquid (ℓ) and solid (s) near the triple point:

$$q_m - q_s \simeq \frac{\rho_\ell}{\rho_s - \rho_\ell}[h_\ell - h_s], \tag{6}$$

$$q_m - q_v \simeq \frac{\rho_s}{\rho_s - \rho_\ell}[h_\ell - h_s]. \tag{7}$$

In both these equations, terms that involve the coexisting 2D gas at the triple point are omitted. They are estimated to contribute 20 K or less to the Xe/graphite differences, using values [30,41] for the triple-point parameters of the 2D

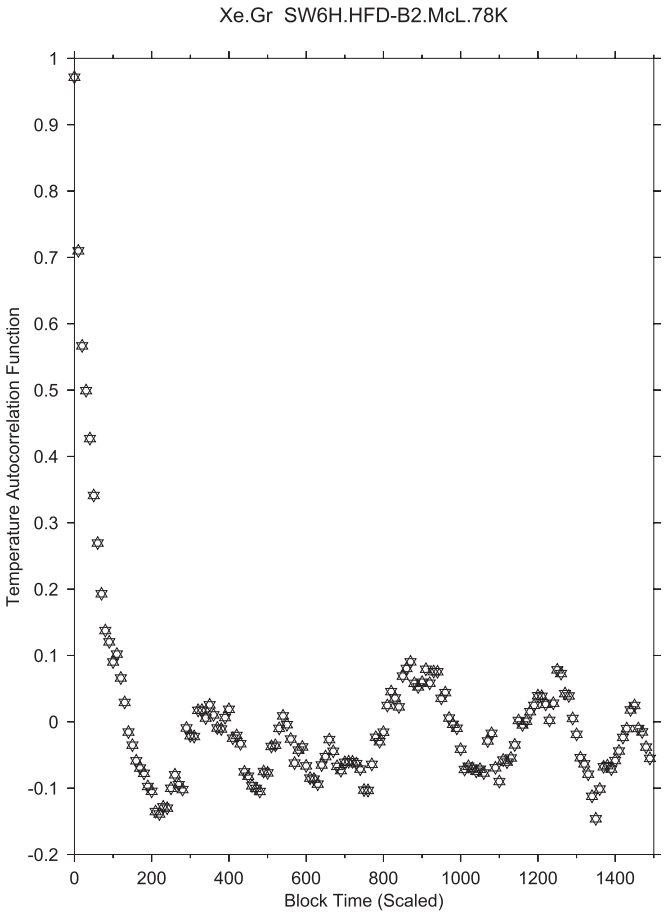

FIG. 9. Time autocorrelation function of kinetic temperature, as defined in Eq. (5) with time "t_n" in the range 500–1000 blocks (1 block = 10 t_0 = 32.6 ps). 78 K patch, with $V_g = -6$ K, $T \simeq 100$ K, very close to melting [31].

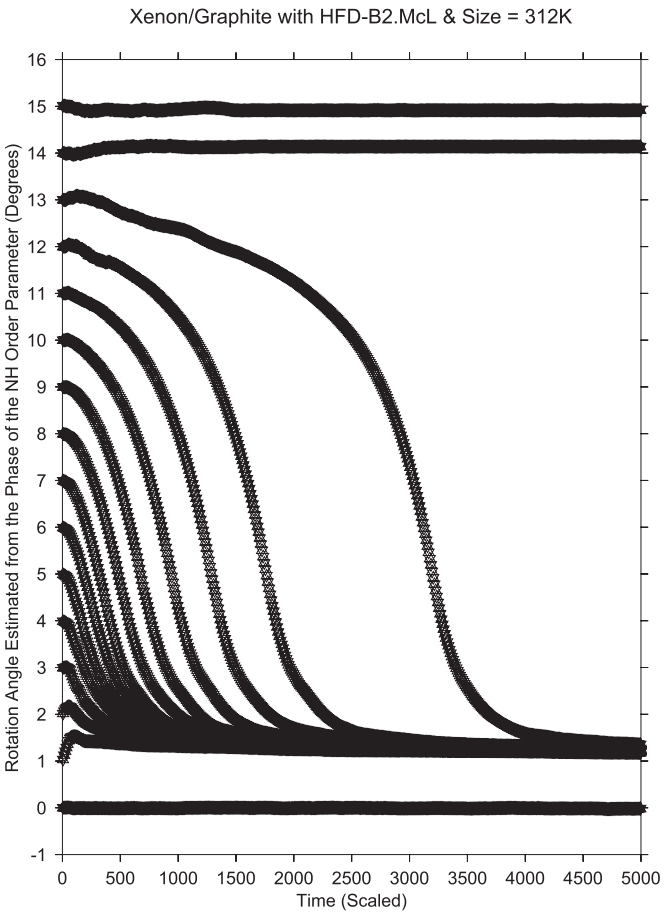

FIG. 10. Relaxation of orientation angle ϑ as a function of scaled time (units of $t_0 = 3.26$ ps) for several initial values of ϑ. The temperature is $T \simeq 10$ K and results are shown for the $V_g = -6$ K 312 K patch. These values of ϑ are derived from the complex phase of ψ_6.

Lennard-Jones (LJ) system. Larher [40] estimated the latent heat of melting at the triple point to be $h_\ell - h_s = 96$ K, using Eq. (7) and the density change at melting on an adsorption isotherm. Tessier [37] reworked the analysis and got a value $\simeq$70 K by using a density change calculated [41] in a simulation of the LJ melting curve. The various experiments [33,37,38] lead to estimates and extrapolated values of $\rho_\ell/\Delta\rho = 8$–25. Hence, in Sec. III B 2, we combine the enthalpy and density changes in our MD simulation to form the ratios in Eqs. (6) and (7) and compare directly to the differences of the empirical heats of adsorption.

The monolayer condenses as an incommensurate solid at least down to [42–44] $T \simeq 15$ K, as reviewed in Paper I. Ellis *et al.* [42] give $L_u = 4.42$ Å at 15 K, a smallest misfit $m = 3.7\%$. The lattice constant data of D'Amico *et al.* [9], Mowforth e*t al.* [43], and Venables *et al.* [45,46] at or near the 2D sublimation curve are shown in Fig. 11.

The threshold misfit for the transition from incommensurate aligned (IA) to incommensurate rotated (IR) monolayer solid is given as $m_c = (1.5 \pm 0.5)\%$ at 65–70 K by Hamichi *et al.* [45] and as $m_c \simeq 1.9\%$ at 70–75 K by Hong *et al.* [44]. Both correspond to compressed monolayer states with $L < 4.35$ Å.

There are several data sets for ϑ as a function of lattice constant L or misfit m. The data of Hong *et al.* [44] were the first to show the reentrant sequence IA $\rightarrow$ IR $\rightarrow$ IA of transitions but clearly are for compressed monolayers. The data of Venables *et al.* [45–47] include cases closer to the sublimation curve and also show the reentrant sequence. The data of D'Amico *et al.* [9] shown in Fig. 4 cover the temperature range 55 to 100 K and the corresponding values of L place the states close to the 2D sublimation curve; we use these as the experimental values corresponding to the states we access in the simulations. There is a consensus [2] that the reentrant sequence of transitions occurs and that the maximum value of ϑ is rather small and in the range 0.5°–1.0°.

It was suggested [48] that Xe/Ag(111) might have densities of 2D gas up to 10% of the solid density at the sublimation curve near the triple point and adsorption isotherm data [49] of Xe/graphite were cited as possible evidence for this. The gas densities observed for Xe/graphite had been attributed [49] to heterogeneities.

B. Results of calculations

1. *Commensurate solid*

We extended the force relaxation calculations [5] to refine the estimates of threshold corrugation amplitudes given in

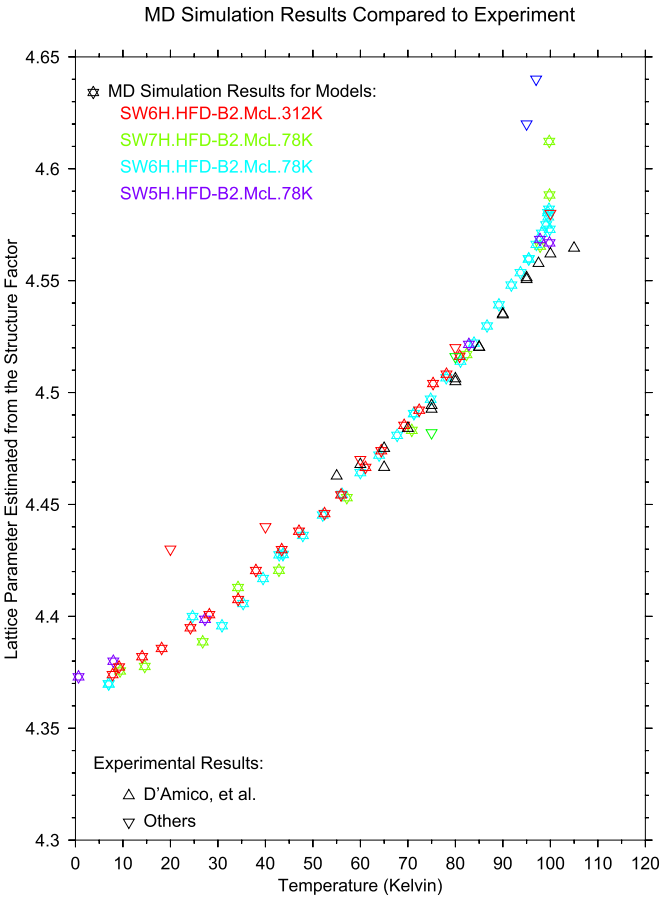

FIG. 11. (Color online) Lattice constant of the unconstrained solid, L_u in Å, as a function of temperature T. L_u is derived from the peak locations of the structure factor $S(\mathbf{q})$ for various corrugations and patch sizes. The results for $V_g = -5, -6, -7$ K for 78 K patch and $V_g = -6$ K for 312 K patch essentially superpose. Experimental diffraction data of D'Amico *et al.* [9] and of Hamichi *et al.* [45]. The deviation between the experiments and calculations below 50 K arises because of the absence of quantum mechanical effects in the MD calculation.

Paper I by using a finer grid of V_g and evaluating the initial slope of the free energy for uniaxially incommensurate lattices at quite small misfit ($m < 0.5\%$). The answers are scarcely changed. The threshold for a classical Xe/graphite monolayer to condense as a commensurate lattice at $T = 0$ K is $V_g = -6.0 \pm 0.1$ K. When zero-point energy is included, the threshold shifts to $V_g = -8.3 \pm 0.1$ K. Thus, the (classical mechanics) MD simulations with $V_g = -7$ K should give a commensurate monolayer as $T \to 0$ K and, indeed, this occurs in the simulations. However, thermal expansion in the $\hbar \to 0$ approximation to the quasiharmonic theory (QHT) leads to a lattice constant 4.33 Å at $T = 10$ K for $V_g = -7$ K.

2. Triple-point melting

The melting temperature for the 78 K and 312 K islands (i.e., unconstrained patches) is $T_t \simeq 100$ K to within ± 1 K. This is set by the extrapolation of the drops in the hexatic order parameter $|\psi_6|$ and the structure factor peak height $S(\tau_0)$ for the leading reciprocal lattice vector (Figs. 1 and 2) and is insensitive to the value of V_g and the size of the patch. The average density also decreases rapidly as T_t is approached, as shown in the Supplemental Material [19]. The calculated drop in $|\psi_6|$ is steep and continuous but is consistent with the experimental assignment of the triple-point melting as first order. It does not exclude an interpretation as a continuous transition [15] although the two transitions of continuous 2D melting on a smooth surface [4] ($V_g = 0$) would have to be spaced by less than ~1 K. The fact that the results for three values of V_g and the Null series superpose closely near the melting is in accord with observations [3] of close similarities in melting phenomena for Xe/graphite and for Xe/Ag(111), nominally a system with very small corrugation effects [50]. The persistence of a tail in $|\psi_6|$ above T_t (Fig. 1) is in accord with the corrugation energy (V_s) acting as a driving field for this order parameter. The drops in $S(\tau_0)$ and ψ_6 occur over a much smaller fractional temperature range than in a simulation [26] of melting at higher 2D pressure and temperature.

The calculated triple-point temperature T_t is in excellent agreement with experiment. To our knowledge, this is the closest that any 2D sublimation curve calculation has come to the experimental melting. The calculated T_t is identical to a value of 100 K obtained from the reduced temperature $T_t^* \simeq 0.408$ for the 2D Lennard-Jones solid [15] using the $\epsilon \simeq 245$ K of the effective pair potential (HFD-B2 + McLachlan) of Xe/graphite [51].

The calculated thermal-average total energy and central density for temperatures close to 100 K are shown in Fig. 12. The latent heat of melting obtained from the near-vertical risers for the $V_g = 0, -5, -6$ K series is 60–80 K, in good agreement with the estimates 96 and 70 K cited in Sec. III A. The scaled density $\rho R_{\min}^2$ at the top of the ($V_g = -6$ K) density drop is approximately 1.04 and, depending on how the rounding at the bottom is treated, we get a factor $\rho_\ell / \Delta\rho \simeq 8.1$–$10.2$ and hence to $q_m - q_s = 610$–650 K, which is at the lower end of the empirical range 640–770 K cited in Sec. III A. The latent heat of melting of Asenjo *et al.* [15] for the LJ solid is $0.296\,\epsilon$ for 36 864 particles, or 72 K with $\epsilon = 245$ K.

The MD simulations for 78 K and 312 K, $V_g = -6$ K, show a slightly different rounding for $|\psi_6|$ and E near the melting transition [(Fig. 6) for E and the Supplemental Material [19] for $|\psi_6|$]. The transition becomes sharper for the larger sample, but has hardly any displacement in temperature.

3. Structure: $L_u(T)$

The calculated lattice constant at 60–100 K along the 2D sublimation curve (Fig. 11) agrees with the experimental data [9,43,45,46]. The $L_u(T)$ from the structure factor peaks for both the 78 K and 312 K patches agree well with each other. Calculations with the quantum-corrected and classical cell models at 50–95 K show that the expansion of L_u by quantum effects is quite small and and decreases from 0.003 to 0.002 Å as T increases. Hence, it is meaningful to make comparisons at the ± 0.005 Å scale between the (classical) MD results and the experimental data for 50–95 K. The calculated values of L_u for the three V_g cases merge to 0.01 Å above 50 K, which accounts for the similarity of data for L_u of Xe/Ag(111) [50] and Xe/graphite.

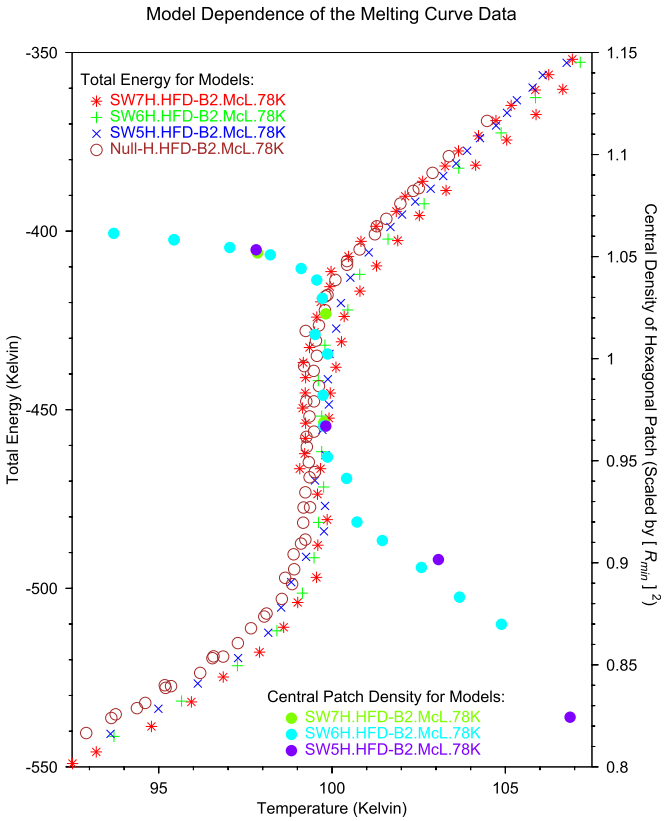

FIG. 12. (Color online) The variation of total energy and central density with temperature near the triple-point temperature. The temperature scale is expanded and the results for several cases are superposed to demonstrate how similar the behaviors are near the melting transition. The two red asterisk series above 100 K are values for heating (lower) and cooling (upper series).

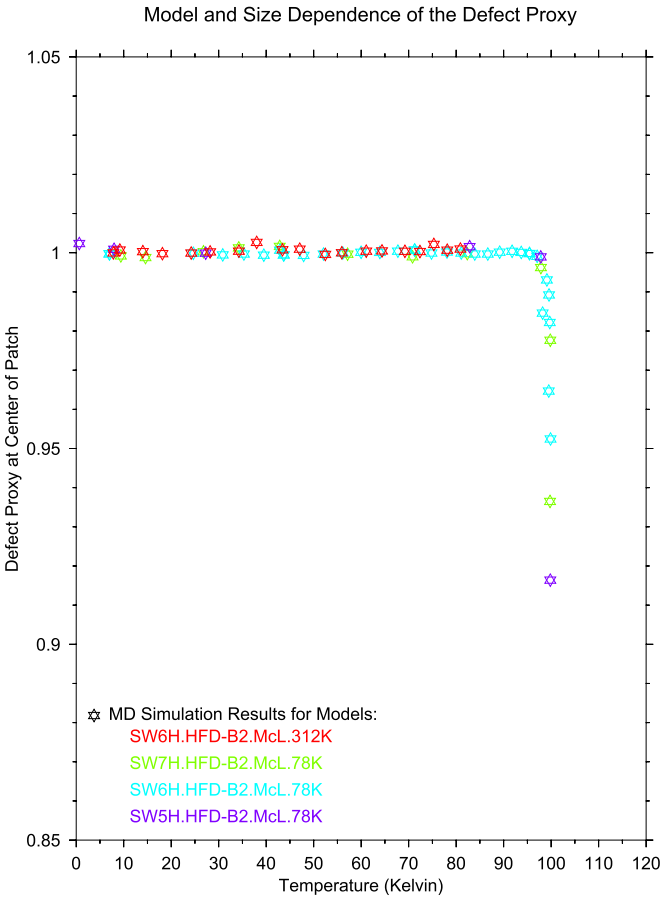

FIG. 13. (Color online) Defect proxy Δ as a function of temperature, $\Delta \equiv \bar{\rho}(L_u^2\sqrt{3})/2$ is constructed from the average density $\bar{\rho}$ at the center of the patch, and the lattice constant L_u determined from structure factor $S(\tau)$. For a perfect triangular lattice, this is precisely 1; Δ remains 1 to within 0.01 until 98 K. V_g and patch size as noted.

Until close to T_t, the lattice has few defects, as shown by the constancy of the product $\Delta \equiv (\bar{\rho}L_u^2\sqrt{3})/2$ at temperatures up to 98 K (Fig. 13). The average density $\bar{\rho}$ is evaluated for a disk of radius $75R_{\min}$ at the center of the patch; for most of the configurations, this is an average over about 19 000 adatoms. L_u is the lattice constant for a diffraction experiment, determined from the peak locations of $S(\tau)$. For a perfect triangular lattice Δ is precisely 1; this is maintained to within 1% until within 1 K of T_t. The vacancy concentration is less than 0.1% at 97 K, but is 0.9% at 99.1 K and 3.8% at 99.5 K. A similar construction [50] using experimental data for Xe/Ag(111) showed that there were fewer than 1% vacancies for the temperature range 56–76 K.

We made a contour analysis of the peaks in the MD data for the structure factor $S(\mathbf{q})$. Over most of the temperature range, until at least 90 K, the peak widths of $S(\mathbf{q})$ are determined by the finite size of the solid patches and the contours are quite circular. At temperatures of 90 to 98 K, the peak widths increase with increasing temperature and the contours become elliptical. However, the azimuthal width is at most 25% greater than the radial width in this regime and so we are not simulating the hexatic phase observed in various x-ray experiments [3,52,53].

We found small-amplitude satellites for the main $S(\mathbf{q})$ peaks at low temperatures (and small misfits). These satellites had the general geometry expected for an incommensurate solid with hexagonal domain structure that is described with mass-density waves. However, they deviated from the simplest description; i.e., although they formed "stars" centered on the sixfold main peaks, most frequently there were four not six satellites in the star. While there might be some effects due to finite size and general disorder in the MD simulation, a similar geometry has been observed in MDW-SCP results. Thus, there is evidence that this is an intrinsic effect of the fundamental domain structure of the system. The intensity in these satellites is correlated with a decrease that is shown in Fig. 2 for the main peak heights of $S(\mathbf{q})$ at low temperatures.

4. *Structure: Orientational epitaxy*

The temperature dependence of ϑ for large xenon islands is complex and in qualitative agreement with experiments [9] (Fig. 4). The ϑ obtained from the MD simulations on unconstrained islands, i.e., along the 2D sublimation curve, decreases as T increases [54] from 0 to 50 K, is relatively insensitive to T between 50 and 90 K, and then goes to zero as $T_t \simeq 100$ K is approached. This behavior is in contrast to the perturbation theory results, where ϑ increases as the nearest-neighbor spacing L_{nn} increases. The MD results

are qualitatively different from the SCP-MDW and QHT approximations at temperatures above 60 K. The difference may arise because increased thermal averaging reduces the effectiveness of a given energy corrugation V_g. This decrease in the importance of the MDW energy term appears to allow an increased role for edge effects along the boundary of the patch. We have not established any systematic difference to the dependence of $\vartheta(T)$ on V_g for the 78 K patches because fluctuations in the inferred ϑ for a given V_g are comparable to the differences between the series. However, fluctuations in the 312 K system are clearly smaller both than those in the 78 K system and than those found in the experimental data (Fig. 4). The results for $\vartheta(T)$ appear to have a smooth variation within these fluctuations.

For the strongly compressed monolayer solid, the solid thermally expands (increasing misfit) from the commensurate lattice to an incommensurate lattice, and there is a temperature range where ϑ increases as T increases. We estimate the threshold (critical) misfit m_c for rotation by using the perturbation-variation (PV) approximation to calculate the ϑ dependence of the modulation energy. E_{MDW} is minimum for the incommensurate aligned IA structure for misfits up to m_c. For $m > m_c$, it is lower at an angle slightly displaced from the 30° azimuth. For $V_g = -5, -6, -7$ K, m_c is 1.4%, 1.6%, and 1.8% in the PV approximation. (SCP results for the evolution of the minimum of E_{MDW} with L for $V_g = -6$ K are shown in the Supplemental Material [19].) The experimental data place the threshold at $m_c \simeq 1.5\%$ for temperatures of 65–75 K and pressures close to the bilayer condensation. Using the PV approximation to E_{MDW} and free energies at 60 K from quasiharmonic theory [5], chemical potential constructions show that the transition IA → IR occurs at a misfit very close to that where the energy minimum moves from 30°. Thus, the calculations reproduce the experimental threshold for values of V_g in the range set by Paper I. The initial stage of the expansion is reproduced by the PV approximation, but the experimental reentrant transition to an IA phase at higher temperatures is not yet reproduced by such approximations.

The tail of $|\psi_6|$ at $T > T_t$ in Fig. 1 arises from the hexatic ordering field h_6 that drives orientational epitaxy and, presumably, also from finite-size effects. We do not know of a theoretical analysis that gives an explicit construction to extract h_6 from the data in Fig. 1.

5. 2D gas

The virial pressure P_v of the patches calculated with Eq. (4) has a very small magnitude and is negative for temperatures below 75 K. The standard deviation of the averages is larger than the average in that range. At $T > 75$ K, P_v is positive and the simulation gives stable values, as shown in Fig. 3. Then, the results for the three nonzero corrugation amplitudes, the Null series ($V_g = 0$), and two patch sizes are very similar and $P_v(T)$ rises steeply with increasing temperature, as is usual for vapor pressure curves. The fact that the results for the four values of V_g are so similar is further evidence that corrugation energy effects are small at these temperatures and solid densities. More quantitatively, the ratio P_v/T corresponds to rather small gas densities for an ideal 2D gas. For the $V_g = -6$ K (78 K) series of simulations, we found the number of adatoms with zero, one, or two neighbors within a radius 6.4 Å, i.e., the populations of monomers, dimers, and trimers. For 75–90 K, the monomer density is less than 1% of the solid density and in fair agreement with the value inferred from P_v/T. For 90–99 K, the combined density of monomers, dimers, and trimers increases until it is about 5% of the solid density at the melting temperature.

These results, with low 2D gas densities up to 90 K, strongly support the assignment by Bienfait *et al.* [49] that the gas they observed just before the monolayer solid condensation of Xe/graphite is an extrinsic effect, probably due to heterogeneities.

6. MD simulation of domains

The domain structure of Xe/graphite was discussed in Paper I. These simulations extend that work to larger systems and, perhaps more importantly, these possess boundaries between the solid and a vapor (below the triple point). Therefore, the solid is not pinned by the boundaries of the box, but is surrounded by the vapor. It is free to rotate in a way that is not possible for the constrained system.

One observed aspect of the vapor-solid boundary is quite striking and ubiquitous. In all simulations, both for the hexagonal patches discussed here and for rectangular patches that are not presented here, the domain walls intersect the patch boundary at right angles. This persists until $T \simeq 80$ K, where the boundaries become rather disorganized. It spans the temperature range 50–80 K where the MD values for ϑ are rather constant. Although we have no model for how this behavior of the walls arises, we believe that it produces an aligning effect that competes with the MDW-driven orientational epitaxy term. As the MDW term is an interior effect and this is a boundary effect, it gives another interior-boundary competition. The boundary effect will be important for the ϑ range where the MDW effects are relatively flat, as they are for $\vartheta = 0°$–$2°$, where the E_{MDW} is near its minimum value. This scenario is bolstered by the observation of twists in the alignment of the rows of atoms as one moves from the patch boundary into the interior. In the interior of the patch, the alignment of atoms appears to be consistent with the epitaxy angle predicted by the MDW theory, at least at low temperature, while close to the boundary there are significant deviations from this. Furthermore, as the temperature is increased, the structure of the domains and domain walls becomes far less ordered, more chaotic, and rather ill defined. We did not carry out any detailed analysis of this effect, so our observations are more qualitative than quantitative. Nevertheless, we conjecture that the alignment of the domain wall at the boundaries contributes to a competition between interior effects (MDW) and size-dependent boundary effects that was already discussed in Sec. II C 3.

Using the criterion [5] that adatoms more than $\ell/4$ from a minimum of V_s are in domain walls, the fraction of adatoms in domain walls increases from 0.585 at 48 K to 0.666 at 98 K, for the 78 K patch with $V_g = -6$ K. A purely random placement of adatoms on the surface would have a fraction 0.73 assigned to walls by this criterion.

IV. CONCLUSIONS

The estimate $V_g \simeq -6$ K still is our best estimate. Recent *a priori* calculations [55] scatter, but are consistent with this value.

A striking aspect of our simulation is that the main precursors of the melting occur over a very narrow temperature range, about 1 K or 1% of the temperature. The hexatic order parameter $|\psi_6|$ drops to about 0.9 as the temperature increases from 20 to 90 K and then there is a steep drop from $\simeq 0.8$ to $\simeq 0.1$ as the temperature increases from 99 to 100 K (Fig. 1). There is a similar steep drop in the structure factor peak values $S(\boldsymbol{\tau})$ for the first three shells of reciprocal lattice vectors (Fig. 2). The concentration of lattice defects also increases sharply in the final approach to the melting temperature (Fig. 13). Similarly, the rise in the energy that we interpret as a latent heat of melting occurs over less than 1 K (Fig. 6). In calculations [15] for a Lennard-Jones model on a smooth surface, relaxation times became very large only within 1% of the melting temperature.

The possibility of continuous melting [17] still is undecided for many monolayer examples. We find the melting of Xe/graphite at the triple point likely is a first-order transition, in agreement with Strandburg's review [16]. We note the possibility that calculations on yet larger samples and carried to even longer times might change this, although our results with $N = 78\,000$ and 312 000 and those of Asenjo *et al.* [15] with $N = 36\,864$ give reduced triple-point temperature and latent heat of melting that lie in the range estimated with an early simulation [30] using $N = 224$.

The x-ray results [9] for the orientational alignment ϑ of Xe/graphite have been a puzzle from the start, as they disagree strongly with a theory that gives a reasonable account of data for other rare gases adsorbed on graphite. Our simulation bridges the gap between the experimental and theoretical results. At low temperatures, it gives an alignment that is close to that from the simplest analytical approximation [6], with small differences that we attribute to boundary effects. At the moderate to high temperatures of the x-ray work [9], the simulation tracks those data with a scatter that is comparable to that in the experiments. We have a coherent explanation for the experimental results. The effects of the MDW energy are reduced by thermal excitations, and at high enough temperature they become less important than other effects, all of which restrict the alignment to be near the 30° azimuth of the graphite. A detailed understanding of these other effects will have to come from future studies of large-scale distortions in the thermally excited monolayer solid.

ACKNOWLEDGMENTS

We thank Lafayette College for its support and the Computer Science Department of Lafayette College for use of their research cluster. We thank J. Bavaresco for her assistance in the structure factor calculations reported here.

APPENDIX A: MD METHODOLOGY

The time step in the MD calculation is $0.01t_0$, where the characteristic time is $t_0 = R_{\min}\sqrt{m_{\mathrm{Xe}}/\epsilon} = 3.26$ ps with the ϵ and $R_{\min}$ of the HFD-B2 Xe-Xe potential [20]. In the dense phases, the calculations of energy and forces generally include 36 atomic neighbors (5 hexagonal shells). The islands had 78 000 Xe atoms for $V_g = 0, -5, -6, -7$ K and 312 000 Xe atoms for $V_g = -6$ K. For most of the temperatures, the cells had large islands of solid surrounded by very low density gas, with an average cell density $\rho R_{\min}^2 \simeq 0.53$. These are relatively large systems even in the context of recent simulations of 2D melting [15,26,28]. The results for the two $V_g = -6$ K series agree well, even within 1 K of the melting temperature.

Thermal averages were done in blocks of 10^3 time steps (=32.6 ps) and final averages typically were formed on blocks 400–500, i.e., at 13–16 ns. Some cases were carried to 600–800 blocks. The evolution of block averages was used to assess the approach to equilibrium. At temperatures above about 75 K, the relaxation of ϑ to a steady value tended to be slow. Also the increased disorder in the Xe islands above 70 K required reconstructing neighbor lists every 25 time steps and this too slowed the simulations. Measures used to assess the approach to equilibrium and evidence for lack of equilibrium, metastability, or hysteresis were described Sec. II C 4.

Gaussian statistical characterization of the values for temperature and total energy indicates the averages have three to four significant figures, i.e., uncertainties smaller than the resolution shown in the figures. The corresponding analysis for the pressure P_v gives ± 0.01 K/Å^2, relatively constant for $T = 50$–100 K. It is difficult to give a quantitative assignment of the uncertainty in the angle ϑ derived from the structure factor because it was formed as an average of values fit to only four peaks (assumed to be those of a hexagonal structure) in $S(\mathbf{q})$. Our estimate is that $\pm 0.1^\circ$ is appropriate for the data shown in Fig. 4, as there likely are non-Gaussian variations and perhaps chaotic effects due to the boundaries.

APPENDIX B: SURROGATES

We have found it convenient to use some surrogates to monitor the progress of the MD calculations before detailed analyses are performed. These are recorded here, as our success with them may be informative to workers in related applications: (1) The nearest-neighbor separation L_{nn} may be estimated by evaluating the average density in a disk of radius $7.5R_{\min}$ at the center of a large patch, before determining the peaks in the structure factor $S(\mathbf{q})$. As shown in the Supplemental Material [19], this gives estimates accurate to $\delta L < 0.005$ Å up to 95 K. The increasing population of vacancies above 95 K was discussed for Fig. 13. (2) The orientational epitaxy angle ϑ may be estimated from the complex phase φ of the hexatic order parameter ψ_6 as $\vartheta = \varphi/6$, before the structure factor calculation, as shown in the Supplemental Material [19]. Since both the real and imaginary parts of ψ_6 go to zero as T_t is approached, this way of estimating ϑ becomes unreliable within 5 K of T_t. (3) We estimated the 2D gas density ρ_g from the virial calculation of the spreading pressure, using $\rho_g = P_v/T$, up to 90 K rather than explicitly counting cluster densities. (4) Although we have not used it here, we estimated the density of fivefold- and sevenfold-coordinated lattice defects by counting the number of nearest neighbors, rather than a Voronoi polyhedra construction.

APPENDIX C: PERTURBATION-VARIATION (PV) APPROXIMATION

We adapt a generalization [56] of the Novaco-McTague perturbation theory [6] to cover lattices with small misfits. The nonlinear response [8] of the monolayer lattice to the corrugation energy is approximated with one shell of Fourier components for the position modulations, although solutions in the SCP-MDW theory at misfits below 0.02 typically include three to five g shells. Thus, the accuracy decreases at misfits less than about 0.01. It remains informative and is computationally simple for most of the states treated here and has been adapted to treat finite-size effects of the Xe patches by constraining the sums in Eq. (C1).

The total potential energy for adatoms at positions $\{\mathbf{r}_j\}$ is

$$\Phi = \sum_i V_s(\mathbf{r}_i) + \sum_{i<j} \phi(|\mathbf{r}_i - \mathbf{r}_j|), \tag{C1}$$

with pair potentials ϕ and the substrate corrugation energy V_s [Eq. (1)]. The dynamical matrix for small-amplitude vibrations about the positions $\{\mathbf{R}_j\}$ in the uniform incommensurate lattice is

$$\mathbf{D}(\mathbf{g}) = \sum_j [1 - \exp(\imath \mathbf{g} \cdot \mathbf{R}_{j0})] \nabla\nabla\phi\,, \tag{C2}$$

with orthonormal eigenvectors $\mathbf{u}_\alpha(\mathbf{g})$ (real for a 2D Bravais lattice):

$$\mathbf{D}(\mathbf{g}) \cdot \mathbf{u}_\alpha(\mathbf{g}) = \lambda_\alpha \mathbf{u}_\alpha(\mathbf{g}), \quad \alpha = 1,2. \tag{C3}$$

Define the trial array of perturbed positions:

$$\mathbf{r}_j = \mathbf{R}_j + \sum_{\alpha=1}^{2} f_\alpha \sum_{\mathbf{g}} \mathbf{u}_\alpha(\mathbf{g})(-\imath V_g) \exp(\imath \mathbf{g} \cdot \mathbf{R}_j) \times [\mathbf{g} \cdot \mathbf{u}_\alpha(\mathbf{g})]/\lambda_\alpha(\mathbf{g}), \tag{C4}$$

where f_1 and f_2 are variational parameters. The angle ϑ that a primitive vector of the uniform adlayer lattice makes with a primitive reciprocal lattice vector $\mathbf{g}(10)$ of the substrate (i.e., the 30° azimuth of the substrate space lattice) is specified for each variational calculation.

We evaluate the total potential energy Φ for the positions $\mathbf{r}_j$ without expanding the functions V_s and ϕ. The scale factors f_α are varied to minimize Φ for each choice of $\{\mathbf{R}_j\}$ at given ϑ. The energy $E(\mathrm{PV})$ is the difference between Φ and the potential energy of the uniform lattice with the same average L_{nn}. The optimal orientation at small misfits is $\vartheta = 0°$, i.e., IA. At larger misfits, there are double minima at angles displaced by $\pm\vartheta$ from 30° and the minimum energy configuration is rotated, i.e., IR.

We test the accuracy of the PV approximation for Xe/graphite lattices with L_{nn} in the range 4.42–4.56 Å, by comparing $E(\mathrm{PV})$ to the energy E_{MDW} obtained by force-relaxation calculations [5] on higher-order-commensurate (HOC) unit cells. Results for several IA and IR lattices are given in Table I. The accuracy of the PV approximation increases as L_{nn} increases. Note that the MD simulations give lattices with $L_{nn} > 4.42$ Å for $T > 40$ K, so that the PV approximation has accuracy for the static lattice value of E_{MDW} that is better than about 6% over most of the range of the simulations. The PV-approximation error increases as ϑ decreases, at nearly constant L_{nn}, as a consequence of the decrease in magnitude of the misfit wave vector. Results for the second-order perturbation-theory [6] values E_{NM} are also shown. The perturbation theory gives the magnitude $|E_{\mathrm{MDW}}|$ for most of the range of separations given in this table, but it overestimates the change in E_{MDW} from the $\sqrt{3}R30°$ alignment to the ϑ that minimizes E_{MDW}. As another series of tests, we compared the $E(\mathrm{PV})$ to $E_{\mathrm{MDW}}(\mathrm{SCP})$ for $V_g = -6$ K and $T = 0$ K and $L = 4.38$,4.39, and 4.41 Å. There was agreement to within 0.3 K out of −4 to −6 K at $\vartheta = 0°$ and 3°.

[1] J. Suzanne and J. M. Gay, in *Physical Structure*, edited by W. N. Unertl (volume editor), Vol. 1 in the Handbook of Surface Science (series editors S. Holloway and N. V. Richardson) (North-Holland, Amsterdam, 1996), Chap. 10, pp. 503–575.

[2] L. W. Bruch, R. D. Diehl, and J. A. Venables, Rev. Mod. Phys. **79**, 1381 (2007), especially Sec. IV. E.1.

[3] N. Greiser, G. A. Held, R. Frahm, R. L. Greene, P. M. Horn, and R. M. Suter, Phys. Rev. Lett. **59**, 1706 (1987).

[4] D. R. Nelson and B. I. Halperin, Phys. Rev. B **19**, 2457 (1979).

[5] L. W. Bruch and A. D. Novaco, Phys. Rev. B **77**, 125435 (2008), denoted Paper I in the text.

[6] A. D. Novaco and J. P. McTague, Phys. Rev. Lett. **38**, 1286 (1977); J. P. McTague and A. D. Novaco, Phys. Rev. B **19**, 5299 (1979).

[7] We define the misfit m as the fractional dilation of the lattice from the $\sqrt{3}R30°$ commensurate lattice constant L_c, $L = L_c(1 + m)$, and usually convert the decimal to percent.

[8] H. Shiba, J. Phys. Soc. Jpn. **48**, 211 (1980).

[9] K. L. D'Amico, J. Bohr, D. E. Moncton, and D. Gibbs, Phys. Rev. B **41**, 4368 (1990).

[10] This arises because the MDW effect is fundamentally a bulk phenomenon associated with the competition between longitudinal (compressional) distortions and transverse (shear) distortions. As a smaller percentage of the monolayer atoms are on the boundaries, the effects of the boundaries become less pronounced. See the discussion in Secs. II C 3 and III B 6.

[11] W. J. Nuttall, D. Y. Noh, B. O. Wells, and R. J. Birgeneau, Surf. Sci. **307–309**, 768 (1994).

[12] A. D. Novaco, Phys. Rev. B **19**, 6493 (1979).

[13] A. D. Novaco, Phys. Rev. B **22**, 1645 (1980).

[14] E. Flenner and R. D. Etters, Phys. Rev. B **73**, 125419 (2006).

[15] D. Asenjo, F. Lund, S. Poblete, R. Soto, and M. Sotomayor, Phys. Rev. B **83**, 174110 (2011).

[16] K. J. Strandburg, Rev. Mod. Phys. **60**, 161 (1988), Sec. IV. D.2.

[17] J. G. Dash, Rev. Mod. Phys. **71**, 1737 (1999).

[18] F. F. Abraham, Phys. Rev. Lett. **50**, 978 (1983).

[19] See Supplemental Material at http://link.aps.org/supplemental/10.1103/PhysRevB.89.125431 for eight additional figures showing size dependence and hysteresis for $|\psi_6|$, size dependence of the P_v, relaxation of ϑ at 53–58 K, SCP-MDW results for

$E_{\mathrm{MDW}}(\vartheta)$ at $L = 4.30$–4.39 Å, the central density as a function of T, and the accuracy of surrogates for L_u and ϑ as well as a table extending Table I to smaller misfit.

[20] A. K. Dham, W. J. Meath, A. R. Allnatt, R. A. Aziz, and M. J. Slaman, Chem. Phys. **142**, 173 (1990); $\epsilon = 282.8$ K; $R_{\mathrm{min}} = 4.3635$ Å.

[21] A. D. McLachlan, Mol. Phys. **7**, 381 (1964).

[22] L. W. Bruch, M. W. Cole, and E. Zaremba, *Physical Adsorption: Forces and Phenomena* (Clarendon, Oxford, 1997) [corrected reprinting (Dover, Mineola, New York, 2007)].

[23] D. Frenkel and B. Smit, *Understanding Molecular Simulation: From Algorithms to Applications*, Computational Science Series, Vol. 1 (Academic, London, 2002); J. M. Haile, *Molecular Dynamics Simulation: Elementary Methods* (Wiley, New York, 1992).

[24] A. D. Novaco and P. A. Shea, Phys. Rev. B **26**, 284 (1982); Fig. 9 shows $|\psi_6|$ as function of energy and with a drop at melting that is not as sharp as here.

[25] The MD evaluation of ψ_6 is straightforward for the corrugated surface $V_g \neq 0$. For the smooth surface, $V_g = 0$, there is a slow rotational drift of the patch. Then, the real and imaginary parts of ψ_6 are evaluated on each time block, with only a small change in orientation, and $|\psi_6|$ is formed for later averaging.

[26] K. Wierschem and E. Manousakis, Phys. Rev. B **83**, 214108 (2011).

[27] C. Udink and J. van der Elsken, Phys. Rev. B **35**, 279 (1987).

[28] H. Shiba, A. Onuki, and T. Araki, Europhys. Lett. **86**, 66004 (2009).

[29] M. P. Allen and D. J. Tildesley, *Computer Simulation of Liquids* (Oxford University Press, New York, 1987), Sec. 2.4.

[30] J. M. Phillips, L. W. Bruch, and R. D. Murphy, J. Chem. Phys. **75**, 5097 (1981).

[31] The temperature for this case is $\langle K \rangle = 99.8$ K and the lattice constant derived from the leading diffraction peak in $S(\mathbf{q})$ is 4.59 Å. The patch is very close to melting, as the (10) peak is down by a factor 100 from the (10) peak at 95.4 K and the g_0 modulation by the graphite substrate gives a stronger peak than both the (10) and (11) peaks of this lattice.

[32] M. D. von Przychowski, H. Wiechert, G. K. L. Marx, and G. Schönhense, Surf. Sci. **541**, 46 (2003).

[33] A. Thomy and X. Duval, J. Chim. Phys. **67**, 1101 (1970).

[34] A. Thomy, X. Duval, and J. Regnier, Surf. Sci. Rep. **1**, 1 (1981).

[35] J. A. Litzinger and G. A. Stewart, in *Ordering in Two Dimensions*, edited by S. K. Sinha (North-Holland, New York, 1980), p. 267.

[36] E. M. Hammonds, P. Heiney, P. W. Stephens, R. J. Birgeneau, and P. M. Horn, J. Phys. C: Solid State Phys. **13**, L301 (1980).

[37] C. Tessier, Ph.D. thesis, Université de Nancy, France, 1984, issued as Report No. CEA-R-5250 (unpublished), Sec. IV. 4; Y. Larher, in *Surface Properties of Layered Structures*, edited by G. Benedek (Kluwer, Dordrecht, 1992), pp. 261–315.

[38] R. Gangwar, N. J. Colella, and R. M. Suter, Phys. Rev. B **39**, 2459 (1989).

[39] P. A. Heiney, P. W. Stephens, R. J. Birgeneau, P. M. Horn, and D. E. Moncton, Phys. Rev. B **28**, 6416 (1983).

[40] Y. Larher, J. Chem. Soc. Faraday Trans. I **70**, 320 (1974).

[41] J. A. Barker, D. Henderson, and F. F. Abraham, Physica (Utrecht) A **106**, 276 (1981).

[42] T. H. Ellis, G. Scoles, U. Valbusa, H. Jónsson, and J. H. Weare, Surf. Sci. **155**, 499 (1985).

[43] C. W. Mowforth, T. Rayment, and R. K. Thomas, J. Chem. Soc. Faraday Trans. II **82**, 1621 (1986).

[44] H. Hong, C. J. Peters, A. Mak, R. J. Birgeneau, P. M. Horn, and H. Suematsu, Phys. Rev. B **36**, 7311 (1987); **40**, 4797 (1989).

[45] M. Hamichi, A. Q. D. Faisal, J. A. Venables, and R. Kariotis, Phys. Rev. B **39**, 415 (1989).

[46] T. E. A. Zerrouk, M. Hamichi, R. H. Milne, J. D. H. Pilkington, and J. A. Venables, Inst. Phys. Conf. Ser. **138**, 221 (1993).

[47] M. Hamichi, R. Kariotis, and J. A. Venables, Phys. Rev. B **43**, 3208 (1991).

[48] J. Unguris, L. W. Bruch, M. B. Webb, and J. M. Phillips, Surf. Sci. **114**, 219 (1982).

[49] M. Bienfait and J. A. Venables, Surf. Sci. **64**, 425 (1977); J. Suzanne, J. P. Coulomb, and M. Bienfait, *ibid.* **44**, 141 (1974).

[50] J. Unguris, L. W. Bruch, E. R. Moog, and M. B. Webb, Surf. Sci. **87**, 415 (1979).

[51] The corresponding estimate for the Flenner-Etters Ar/graphite simulation [14] is less accurate. Scaling the effective potential minimum $\epsilon \simeq 128$ K by $T_t^* = 0.408$ gives $T_t = 52$ K while the simulation gave $T_t = 49$ K.

[52] T. F. Rosenbaum, S. E. Nagler, P. M. Horn, and R. Clarke, Phys. Rev. Lett. **50**, 1791 (1983).

[53] S. E. Nagler, P. M. Horn, T. F. Rosenbaum, R. J. Birgeneau, M. Sutton, S. G. J. Mochrie, D. E. Moncton, and R. Clarke, Phys. Rev. B **32**, 7373 (1985).

[54] The low-temperature MD values of ϑ are in fair agreement with perturbation-theory results, when the MD values are compared to zero-temperature calculations at the same lattice constant. At $T = 20$ and 40 K, with $L = 4.38$ and 4.415 Å, the angles are $\vartheta_{\mathrm{MD}} = 0.8^\circ$–$1.0^\circ$ and 0.4°–0.6°, respectively. The SCP-MDW values ($V_g = -6$ K) are $\vartheta_{\mathrm{SCP}} = 0.6^\circ$ and 0.9°, while the original perturbation theory gives $\vartheta_{\mathrm{NM}} = 0.9^\circ$ and 1.1°, respectively.

[55] L. Sheng, Y. Ono, and T. Taketsugu, J. Phys. Chem. C **114**, 3544 (2010); A. Ambrosetti and P. L. Silvestri, *ibid.* **115**, 3695 (2011).

[56] L. W. Bruch and J. Z. Larese, Phys. Rev. B **85**, 035401 (2012).